water

MDPI

Article

Producing Efficient Adsorbents from Kraft Lignin for the Removal of Contaminants from Water—A Full Factorial Design

Tayra R. Brazil [1,2], Érika M. L. Sousa [2], Erick G. R. dos Anjos [1], Nayara K. Moura [1], Luciana S. Rocha [2], Vânia Calisto [2,*], Maraísa Gonçalves [1] and Mirabel C. Rezende [1]

[1] Science and Technology Institute, Federal University of São Paulo, São José dos Campos 12231-280, SP, Brazil; tayrabrazil@ua.pt (T.R.B.); erick.anjos@unifesp.br (E.G.R.d.A.); nayara.koba.de.moura@gmail.com (N.K.M.); goncalves.maraisa@unifesp.br (M.G.); mirabelcr@gmail.com (M.C.R.)

[2] Department of Chemistry and CESAM, University of Aveiro, 3810-193 Aveiro, Portugal; erikamsousa@ua.pt (É.M.L.S.); lrocha@ua.pt (L.S.R.)

* Correspondence: vania.calisto@ua.pt

Abstract: This work aimed at optimizing the preparation of activated carbon (AC) from Kraft lignin for the adsorption of methylene blue (MB) and amoxicillin (AMX) from water. A full factorial design of three factors (precursor:activating agent (H_3PO_4) ratio, pyrolysis temperature, and residence time) at two levels was used to optimize the AC production. Eight AC products were obtained and evaluated considering the following responses: product yield, specific surface area (S_{BET}), energy consumption, and adsorptive removal of the contaminants under study. The produced AC presented satisfactory S_{BET}, ranging between 750 and 1335 $m^2\ g^{-1}$, and efficient adsorption of MB and AMX from water, achieving up to 99% removal under the studied experimental conditions (100 mg L^{-1} of MB and AMX solution and material dose of 1 g L^{-1}). Statistical analysis showed that product yield and energy consumption for AC production were influenced by temperature and residence time. The determination of a desirability function indicated a precursor/H_3PO_4 ratio of 1:2, pyrolysis at 700 °C, and residence time of 60 min as the optimal production conditions. The optimized AC presented S_{BET} 1335 $m^2\ g^{-1}$ and maximum adsorption capacity of 210 and 280 mg g^{-1} for MB and AMX, respectively.

Keywords: Kraft lignin; chemical activation; pyrolysis; activated carbon; water treatment

check for updates

Citation: Brazil, T.R.; Sousa, É.M.L.; dos Anjos, E.G.R.; Moura, N.K.; Rocha, L.S.; Calisto, V.; Gonçalves, M.; Rezende, M.C. Producing Efficient Adsorbents from Kraft Lignin for the Removal of Contaminants from Water—A Full Factorial Design. *Water* **2024**, *16*, 1838. https://doi.org/10.3390/w16131838

Academic Editor: Laura Bulgariu

Received: 16 May 2024
Revised: 20 June 2024
Accepted: 21 June 2024
Published: 27 June 2024

Copyright: © 2024 by the authors. Licensee MDPI, Basel, Switzerland. This article is an open access article distributed under the terms and conditions of the Creative Commons Attribution (CC BY) license (https://creativecommons.org/licenses/by/4.0/).

1. Introduction

Biomass is an abundant carbon-rich resource with high energy content [1]. Thus, the utilization of biomass for different applications has received special attention as a renewable resource, since it helps to reduce greenhouse gases and can be transformed through efficient physicochemical treatments into bio-oil, hydrogen-rich syngas, and activated carbon (AC) [2,3]. Biomass is mainly composed of lignin, cellulose, and hemicellulose and their relative contents depend on the source of the biomass material [4]. For lignocellulosic materials, the proportion of lignin in the composition of dried biomass ranges from 15 to 40% [5]. Lignin is a renewable raw material characterized by a highly branched polymeric structure with functional groups such as hydroxyl, methoxyl, carbonyl, and carboxylic [6–8]. Approximately 130 million tons of Kraft pulp are available worldwide, with an estimated 70 million tons available for valorization resulting from pulp and paper industries [9–11]. Nowadays, this abundant biomass is considered a waste and is directly burned to produce energy. To date, only 2% of lignin is applied industrially to produce materials with high added value [12]. Thus, the development of new lignin-based materials is an interesting approach, not only to diversify products and markets but also to maintain cost-effective processing of industrial wastes and encourage their reuse as an essential strategy for developing a more circular economy [13–15].

AC can be obtained from carbon-rich precursors, resulting in materials with high surface area and well-developed microporous structure, whose main application is their use as adsorbents for the removal of pollutants from liquid and gaseous phases [16]. These materials can be produced by chemical, physical, or combined activation. Chemical activation involves impregnating the precursor with an acidic or basic reagent, which influences the thermal decomposition of the material and the formation of microporosity, that occurs in a subsequent high temperature treatment at inert atmosphere. Physical activation consists of a heat treatment step of the precursor in an inert atmosphere (carbonization) followed by a second stage at higher temperature in the presence of an activating atmosphere [17,18].

According to the literature, the global AC market reached USD 8.94 billion in 2022, and is projected to reach USD 11.79 billion by 2026 [19]. Currently, one of the most important challenges for the wide application of AC is the decrease in its production cost and sustainability, namely, through the use of agricultural by-products as precursors [20,21]. The available literature reflects a growing interest of the scientific community in exploring the use of lignin for AC production. This interest arises from its wide range of potential applications, ranging from its effectiveness as a pollutant adsorbent in various environmental remediation processes [13] to energy storage through supercapacitors [11].

The use of AC as an adsorbent for contaminant removal can help to mitigate water contamination, which is a significant environmental concern. Among organic microcontaminants, methylene blue (MB) and amoxicillin (AMX) stand out. MB and AMX were selected as representative organic contaminants for the following reasons: MB is one of the most commonly found cationic dyes that is environmentally toxic, persistent, carcinogenic, and mutagenic [22,23]. It is commonly applied as a synthetic dye for dyeing fabrics in the clothing and textile industries. AMX is an antibiotic from the aminopenicillin family used worldwide to control infectious diseases and may be excreted to a significant extent as the parent compound itself or its metabolites, being easily found in the environment and contributing to the increase in antimicrobial resistance. In addition, the European Union (Decision 2020/1161/EU) has included AMX on the list of substances to be monitored due to the risk to the aquatic environment [24]. In this sense, several advanced treatment methods have been developed to eliminate micropollutants from the environment, including adsorption, photocatalysis, ozonation, electrochemical oxidation, and membrane filtration [25–27]. Among these methods, adsorption is particularly interesting due its cost-effectiveness, possible regeneration of the adsorbent, and ease of application [28]. Several studies focus on the study of adsorption using AC to remove MB and AMX from contaminated water. As an example, Dimbo et al. (2024) produced AC from *Spathodea campanulata* with a specific surface area of 1054 $m^2\ g^{-1}$ and maximum adsorption capacity for MB of 90 mg g^{-1} [29]. Jawad et al. (2021) obtained an AC from sugarcane bagasse waste using KOH as an activating agent, resulting in AC specific surface area of 709 $m^2\ g^{-1}$ and adsorption capacity for the MB dye of 136.5 mg g^{-1} [30]. Franco et al. (2017) studied AMX removal using commercial AC and obtained a maximum adsorption capacity of 4.4 mg g^{-1} [31]. Belhachemi and Djelaila (2017) compared the adsorption capacities of commercial AC and AC derived from date pits. Their findings showed that the synthesized AC had higher adsorption capacities, likely due to its significantly larger surface area, reaching up to 1325 $m^2\ g^{-1}$ [32].

In the context of the circular economy, this study aims to investigate the conversion of an industrial by-product into added-value carbon materials with further application in the removal of organic microcontaminants, namely, MB and AMX, from water. By focusing on these two different types of contaminants, this study aims to evaluate the versatility of the produced AC in treating aqueous matrices contaminated with distinct pollutants, which is critical for real-world water purification applications. In a previous study, the carbon samples derived from Kraft lignin were obtained without chemical impregnation of the precursor, resulting in adsorbents with much lower surface areas (287 $m^2\ g^{-1}$) [33]. In another work, AC from Kraft lignin was obtained through impregnation with phosphoric acid and by pyrolysis under a synthetic air atmosphere [34]. The promising results obtained

in that approach were a motivation to deepen the study by now evaluating the effect of pyrolysis under an inert atmosphere, allowing comparison of the results achieved with different approaches. This comparison is crucial as it can reveal significant differences in the properties and removal efficiency of the produced AC, which has not been extensively explored before. For this purpose, the production of AC from Kraft lignin was carried out using a design of experiments (DOE) through a factorial design. DOE is a simple statistical tool widely used to reduce the number of experiments in an optimization process, allowing systematization of the influence of each parameter and interactions between them and the optimization of the process for a given response. In this study, the optimization of AC production involved assessing the impact of three variables: precursor:activating agent ratio, residence time, and pyrolysis temperature. The influence of these variables on different properties was tested, including specific surface area (S_{BET}), product yield (%), energy consumption (Wh), and adsorptive removal of MB and AMX from water. The obtained AC was subsequently characterized and applied in equilibrium and kinetics studies to carry out a first evaluation of the adsorptive performance of the material produced under optimized conditions towards these contaminants.

2. Materials and Methods

2.1. Reagents and Chemicals

For chemical activation for AC production, phosphoric acid was used (H_3PO_4, 85.0%, Sigma Aldrich, Saint Louis, MO, USA). Pyrolyzed materials were washed with hydrochloric acid (HCl, 37.0%, Honeywell Fluka, Charlotte, NC, USA). HCl (37.0%, Honeywell Fluka, Charlotte, NC, USA), sodium hydroxide (NaOH, 99.3%, José Manuel Gomes dos Santos, Odivelas, Portugal), and sodium chloride (NaCl, ≥99.5%, Fluka, Charlotte, NC, USA) were used for determining the point of zero charge (PZC).

MB (≥97.0% Sigma Aldrich, Saint Louis, MO, USA) and AMX (≥99.0% Sigma Aldrich, Saint Louis, MO, USA) were used in adsorption tests. Their molecular structure and some physicochemical properties are presented in Table S1 of the Supplementary Materials. All solutions were prepared with ultrapure water produced in a Purelab Flex 4 system (Elga Veolia, High Wycombe, UK).

2.2. Preparation of the Activated Carbon—Full Factorial Design and Statistical Analysis

Kraft lignin was supplied by Fibria Celulose S.A. Co. (São Paulo, Brazil). A full factorial design 2^3 (three variables and two levels) was applied to support the selection of the optimal conditions for producing AC from Kraft lignin, resulting in 8 AC samples. The selected variables were temperature of pyrolysis (TP), residence time (RT), and impregnation ratio (IR). Firstly, the lignin was impregnated with H_3PO_4 using 1:1 or 1:2 precursor:activating agent ratio (*w*/*w*). Afterwards, impregnated lignin was pyrolyzed at 500 °C or 700 °C during 60 or 180 min, using a tubular oven (EDG) under nitrogen flow at 100 cm^3 min^{-1}. The temperatures of 500 °C and 700 °C for pyrolysis were selected based on values commonly reported in the literature [35–38]. Studies have shown that these temperatures are effective for the activation of lignin and other lignocellulosic materials with phosphoric acid, leading to optimal pore development and adsorption properties. Also, higher temperatures were avoided to maintain the process as sustainable as possible in terms of energy consumption.

The produced AC was washed in two steps. First, a 1 M HCl solution was used, and then distilled water until the washing leachate reached a neutral pH. The HCl concentration was selected based on previous literature studies [39–41]. Then, the samples were dried at 100 °C during 24 h and passed through a 100-mesh sieve to obtain a uniform powder. The described AC production was based on a similar methodology optimized in a previous work [34], but now evaluating the process under an inert as opposed to an oxidizing atmosphere. The samples were named according to the production variables: ACx-y-z, with x, y, and z being the temperature of pyrolysis, residence time, and impregnation ratio, respectively. Example: $AC_{500\text{-}60\text{-}1:1}$ means the sample was obtained at a temperature of

500 °C, residence time of 60 min and precursor:acid mass ratio 1:1. Table 1 presents an overview of the experimental conditions utilized to prepare each AC.

Table 1. Experimental conditions used to produce AC.

Samples	Temperature of Pyrolysis (°C) (TP)	Residence Time (min) (RT)	Impregnation Ratio (wt./wt.) (IR)
$AC_{500\text{-}60\text{-}1:1}$	500	60	1:1
$AC_{700\text{-}60\text{-}1:1}$	700	60	1:1
$AC_{500\text{-}180\text{-}1:1}$	500	180	1:1
$AC_{500\text{-}60\text{-}1:2}$	500	60	1:2
$AC_{500\text{-}180\text{-}1:2}$	500	180	1:2
$AC_{700\text{-}60\text{-}1:2}$	700	60	1:2
$AC_{700\text{-}180\text{-}1:1}$	700	180	1:1
$AC_{700\text{-}180\text{-}1:2}$	700	180	1:2

2.2.1. Responses

The responses considered to carry out the statistical analysis were (i) product yield (%) calculated by Equation (1), (ii) S_{BET} ($m^2\ g^{-1}$) and total pore volume ($V_{0.98}$) (V), (iii) energy consumption (Wh), and (iv) percentage of adsorption of MB and AMX.

(i) Product yield

The product yield (%) was calculated for all materials using Equation (1):

$$Yield = \frac{M_f}{M_i} \times 100\% \quad (1)$$

where M_f is the final mass of each AC sample produced (after pyrolysis, washing, and drying) and M_i is the initial mass of the precursor.

(ii) Specific surface area and total pore volume

Nitrogen adsorption–desorption experiments were performed in a Quantachrome model Nova Win instrument to determine the S_{BET}, pore distribution, and $V_{0.98}$ (pore volume assessed at a pressure of 0.98, which is the standard pressure utilized in nitrogen adsorption and desorption analysis) of the produced AC. The samples were degassed at 300 °C for 2 h. S_{BET} was calculated from the Brunauer–Emmett–Teller equation and the pore size distribution was determined based on Density Functional Theory (DFT). The DFT method allows for determining effective pore size distributions from nitrogen adsorption isotherm data. Characterization measurements require the full isotherm, which ranges from approximately $p/p_0 = 0.04$ to $p/p_0 = 0.99$ for the adsorption method [42].

(iii) Energy consumption—Technical-economic analysis

The operational cost to produce AC was evaluated by estimating the electric energy consumption, depending on the temperature and time used in each synthesis procedure.

(iv) Percentage of adsorption of MB and AMX

Adsorption experiments were carried out to evaluate the efficiency of the produced AC in removing MB and AMX from aqueous media. Solutions of MB and AMX prepared in ultrapure water with an initial concentration (C_i) of 100 mg L^{-1} were used. A volume of 10 mL of each individual MB and AMX solution was put in contact with 10 mg of each AC and stirred for 24 h at 120 rpm, at a controlled temperature of 25 °C. Then, aliquots were withdrawn from stirred tubes at predefined times, and centrifuged for 15 min at 2000 rpm. The supernatants were collected, and the remaining contaminant concentration (C_f) was immediately analyzed. The analytic quantification of MB and AMX was performed by UV/visible molecular spectroscopy (Jasco V-730), at 665 and 228 nm, respectively. The wavelengths of 665 and 228 nm were chosen for UV measurement after a spectrum scan analysis, corresponding to the wavelengths with maximum for absorption

for each pollutant. All the adsorption experiments were performed in triplicate. Control samples (C_0) with the same C_i (100 mg L^{-1} of either MB or AMX) but no AC were also performed as a reference to obtain the adsorption percentages (Adsorption, %) of each contaminant, using Equation (2):

$$Adsorption = \frac{C_0 - C_f}{C_0} \times 100\% \quad (2)$$

where: C_f (mg L^{-1}) is the final concentration of the contaminant after stirring and C_0 (mg L^{-1}) is the concentration of the contaminant in the control.

2.2.2. Analysis of Variance and Desirability Function

ANOVA (analysis of variance) was used to determine the effects of the variables on the responses, considering a confidence level of 95%. Therefore, *p*-values allowed to verify the significance of each factor in the responses. *p*-values ≤ 0.05 and >0.05 point to significant and non-significant factors, respectively. To optimize the process, a desirability function scale ranging from 0 to 1 for each response was employed based on the measured properties. For this, the measured properties of each response were transformed in a dimensionless desirability scale [43]. The statistical analyses were performed using MINITAB software 18.

2.3. Physico-Chemical Characterization of the Optimized Activated Carbon

The optimized AC, selected from the statistical analysis carried out in Section 2.2.1, was further characterized for the evaluation of its morphological, chemical, and physical features.

The morphology of the selected AC was evaluated using field emission gun-scanning electron microscopy (FEG-SEM, FEI equipment, Inspect model). Energy dispersive X-ray spectroscopy (EDS) coupled to the FEG-SEM allowed the determination of the elemental composition and the elemental mapping analysis. Prior to the analysis, the samples were coated with a thin layer of gold.

Fourier transform infrared spectroscopy (FT-IR, PerkinElmer, Spectrum One) using potassium bromide disks, over the range between 4000 and 600 cm^{-1}, with a resolution of 4 cm^{-1} and 20 scans was used to evaluate the functional groups of AC samples.

The structure of optimized AC was investigated by Raman spectroscopy (Horiba equipment, model Olympus) with a laser source at 532 nm, in a spectral interval from 800 to 2000 cm^{-1}.

X-ray diffraction (XRD) (Rigaku Ultima IV automatic diffractometer), with Cu Kα radiation (λ = 1.54178 Å), 40 kV, 30 mA, in the 2θ range of 10 to 50°, at 10° min^{-1}, was used to characterize the crystalline structure of AC. The interplanar distance (d_{002}) calculation used the Bragg Equation [44]. The height of AC crystallite (Lc) and width of crystallite (La) were obtained from the Scherrer Equation [18].

The thermal stability was investigated by thermogravimetric analysis (TGA, NETZSCH, 209 F1 Phoenix) in the interval of 25 to 1000 °C, at a heating rate of 10 °C min^{-1}, under nitrogen and synthetic air atmospheres (20 mL min^{-1}).

PZC was determined by batch equilibration using the drift method. For this purpose, 0.1 M NaCl solutions with pH ranging between 2 and 11 were prepared. Initial pH values (pH_i) were adjusted with 0.1 M and 0.01 M HCl and/or 0.1 M and 0.01 M NaOH. Then, 10 mL of each pH solution (under N_2 atmosphere) were transferred to polypropylene tubes containing 10 mg of AC (final dosage of 1000 mg L^{-1}) and shaken at 80 rpm for 24 h. The final pH (pH_f) was measured and the PZC was determined by plotting ΔpH ($pH_f - pH_i$) vs. pH_i. The PZC is obtained at the *x*-axis interception of the obtained curve ($pH_i = pH_f$) [45].

2.4. Kinetic and Equilibrium Experiments and Modeling

According to the results discussed in Section 3.1, one AC sample was selected for the kinetic and equilibrium studies.

2.4.1. Kinetic Experiments

The time at which each system reached the adsorption equilibrium was determined by shaking single solutions with a specific adsorbent dose during times varying between 5 and 360 min. For this purpose, 1 g L^{-1} of the selected AC was used. The experimental conditions used in the batch experiments are the same as those described in topic (iv) of Section 2.2.1. After shaking, the MB and AMX adsorbed at each time (q_t, mg g^{-1}) was determined according to Equation (3).

$$q_t = \frac{(C_0 - C_t)\, V}{m} \tag{3}$$

where C_0 and C_t (mg L^{-1}) represent the control concentration and the concentration at time t of organic contaminant, respectively; V (L) is the volume of MB or AMX solutions; and m (g) is the mass of AC.

Considering reaction-based models, the pseudo-first-order (Equation (4)), pseudo-second-order (Equation (5)), and Elovich (Equation (6)) mathematical models were used to fit the experimental data [46–48]:

$$q_t = q_e\left(1 - e^{-k_1 t}\right) \tag{4}$$

$$q_t = \frac{q_e^2 k_2 t}{1 + q_e k_2 t} \tag{5}$$

$$q_t = \frac{1}{\beta}(\alpha\beta t + 1) \tag{6}$$

where q_t (mg g^{-1}) is the quantity of MB or AMX adsorbed *per* mass unit of the AC at each time t; t (min) is the contact time between the AC and MB or AMX; q_e is the concentration of contaminant adsorbed at equilibrium/mass unit of the AC (mg g^{-1}); k_1 (min^{-1}) and k_2 (mg^{-1} min^{-1}) are the pseudo-first- and pseudo-second-order rate constants, respectively; α (mg g^{-1} min^{-1}) and β (g mg^{-1}) are the initial adsorption rate and desorption constant, respectively.

2.4.2. Equilibrium Experiments

Equilibrium adsorption tests were carried out by shaking 1 g L^{-1} of AC with single solutions of MB and AMX with concentrations ranging from 25 to 1000 mg L^{-1}. The experimental conditions used in the batch experiments are the same as those described in topic (iv) of Section 2.2.1. Afterward, the amount of MB and AMX in the aqueous phase was determined, the concentration of contaminant adsorbed at equilibrium (q_e, mg g^{-1}) was calculated by Equation (7), and the experimental results were fitted to two non-linear models usually applied to describe the adsorption equilibrium isotherms: the Langmuir [49] and Freundlich [50] models, represented by Equations (8) and (9), respectively:

$$q_e = \frac{\left(C_0 - C_f\right) V}{m} \tag{7}$$

$$q_e = \frac{q_m K_L C_e}{1 + K_L C_e} \tag{8}$$

$$q_e = K_F C_e^{\frac{1}{n}} \tag{9}$$

where C_0 and C_f (mgL^{-1}) represent the control and equilibrium concentrations, q_m is the maximum adsorbed concentration of adsorbate at the equilibrium (mg g^{-1}), K_L is the Langmuir equilibrium constant (L mg^{-1}), $1/n$ is the non-linearity coefficient of the Freundlich isotherm, and K_F is the Freundlich equilibrium constant (mg g^{-1} (L $mg^{-1})^{1/n}$).

3. Results

3.1. Full Factorial Design: Responses

The responses obtained by the full factorial design (namely pore distribution, S_{BET}, yield, and energy consumption to prepare the Acs, and the concentration (%) of adsorbed AMX and MB) are shown in Figure 1 and Table S2 of the Supplementary Materials.

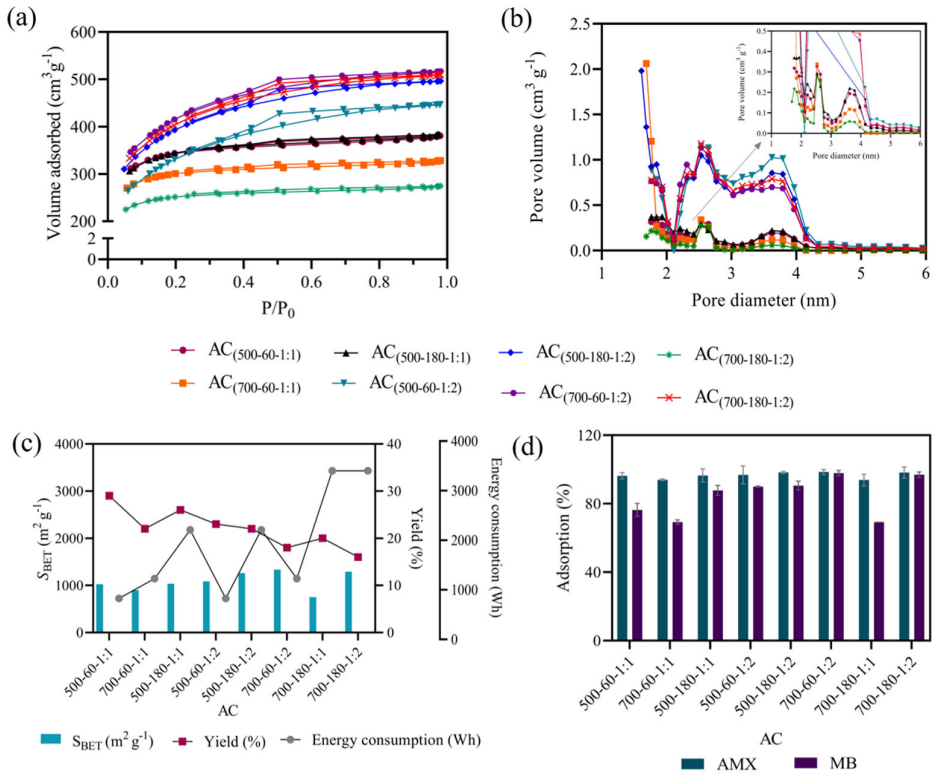


Figure 1. N_2 adsorption/desorption isotherms (**a**), pore distribution (**b**), S_{BET}, yield, and energy consumption for the produced AC (**c**), and the percentage of adsorption of MB and AMX (**d**). (Conditions: 100 mg L^{-1} solution, material dose of 1 g L^{-1}, 120 rpm for 24 h at room temperature).

Analyzing the yield (%), obtained by Equation (1), the results show a decrease as the temperature increases (from 500 °C to 700 °C). The highest yield (29%) was obtained for $AC_{500\text{-}60\text{-}1:1}$ (produced under lower temperature (500 °C) and residence time (60 min) (see Table S2).

Concerning the pyrolysis temperature, the yields ranged between 22 and 29% and 16 and 22% for samples obtained at 500 °C and 700 °C, respectively. As the temperature increases (as well as the amount of activating agent and the pyrolysis time), the material undergoes greater decomposition due to higher volatilization rates, consequently leading to a decrease in yield [39,41]. Yorgun and Yildiz (2015) reported that the yield of AC from Paulownia wood was negatively impacted by a high impregnation ratio of H_3PO_4 activating agent and a high carbonization temperature [51]. Gueye et al. (2014) also observed a similar behavior, showing that the temperature increases from 400 °C to 700 °C resulted in a decrease in yield of approximately 10% [52]. The role of the H_3PO_4 as activating agent is to promote the cleavage of the aryl ether bond of lignin [53]. As a result, the process of conversion of lignin into AC is enhanced, i.e., lower temperatures and times are required.

The S_{BET} of the samples were obtained by nitrogen adsorption and desorption isotherms, shown in Figure 1a. According to the classification of the International Union of Pure and Applied Chemistry (IUPAC), all isotherms presented a combination of types I and IV [54]. The type I isotherm shows adsorption at low pressures and appears in microporous materials (<2 nm). On the other hand, the type IV isotherm presents hysteresis at high pressures and occurs in mesoporous materials (2–50 nm). These results indicate that the samples

have heterogeneous pores, that is, the AC produced has micro- and mesopores. This result is in agreement with the literature, as the heterogeneity of the pores is characteristic of samples treated with H_3PO_4 [19].

Figure 1b shows the pore size distribution within the 1–8 nm range, confirming the presence of both micro- and mesopores structures, with distinct variations in $V_{0.98}$. Consequently, an increase in S_{BET} correlates with a corresponding increase in $V_{0.98}$. This becomes evident when comparing the S_{BET} and $V_{0.98}$ of samples $AC_{700\text{-}60\text{-}1:2}$ (1335 m^2 g^{-1} and 0.80 cm^3 g^{-1}) and $AC_{700\text{-}180\text{-}1:1}$ (750 m^2 g^{-1} and 0.42 cm^3 g^{-1}). Knowing that porous materials are suitable for adsorption, according to the literature [55,56], it is extremely relevant to know the pore size of the adsorbents to determine the best application. Generally, mesoporous materials are used for the adsorption of contaminants in solution, and microporous materials are more suitable for gas adsorption [57].

According to the results presented in Figure 1c, S_{BET} from 750 to 1335 m^2 g^{-1} were achieved for ACs produced in this study. This is within the range of S_{BET} values for AC reported in the literature (500–2000 m^2 g^{-1}) [58]. Therefore, Kraft lignin was converted into AC with a reasonable S_{BET}, regardless of the considered factor levels. The results confirm that the ACs obtained in this study under a nitrogen atmosphere exhibit slightly higher S_{BET} values than those obtained with synthetic air atmosphere in a previous study in which S_{BET} values between 580 and 1220 m^2 g^{-1} were achieved [34]. This occurs due to the presence of oxygen in the synthetic air, which promotes an increase in the speed of the carbonization reactions, leading to the collapse of the pores and, consequently, a decrease in the S_{BET}. Harimisa et al. (2023) investigated the impact of argon, limited air, and vacuum atmospheres on the S_{BET} of AC derived from bamboo. Among the tested atmospheres, air proved to be the least effective, while argon demonstrated the highest efficiency in enhancing S_{BET} [59], which is completely in line with the results obtained for Kraft lignin.

Subsequently, all samples under study were tested as adsorbents for the application in MB and AMX removal. Figure 1d shows the adsorption percentages as a first indication of the adsorption efficiency of the produced materials. The results show that all produced AC samples can adsorb a significant amount of contaminant (using an adsorbent dosage of 1 g L^{-1}), with adsorption (%) of MB and AMX around 97% and 98% for $AC_{700\text{-}180\text{-}1:2}$, respectively. $AC_{700\text{-}180\text{-}1:1}$ adsorbed 69% and 94% for AM and AMX, respectively, and the adsorption efficiency decrease may be related to the lowest S_{BET} value (750 m^2 g^{-1}) obtained for this material (see Table S2). Furthermore, the adsorption (%) is globally higher for MB than for AMX, which achieved adsorption (%) of almost 100% for all samples.

The energy consumption involved in the process of obtaining AC at the tested lab-scale ranged from 726 to 3432 Wh, with longer periods and temperatures resulting in higher energy consumption, as presented in Figure 1c.

3.2. Full Factorial Design: Statistical Analysis and Model Fitting

ANOVA was applied to determine the significant factors that affect the selected responses. The results are presented in Table 2.

The factors analyzed were residence time, temperature of pyrolysis, and precursor:activating agent ratio. Table S2 shows the results of the selected responses (yield of production (%), S_{BET} (m^2 g^{-1}), energy consumption (Wh), and % of adsorption of MB and AMX).

Table 2 shows the results from ANOVA with linear terms utilized to identify which factors influence each response. All responses presented one or more significant factors, as they obtained a p-value < 0.05, for a confidence level of 95%. The significance of each factor was also evaluated based on the sum of squares (SS).

Table 2. Analysis of variance (ANOVA) for each evaluated response at 95% confidence level.

Responses	Factors [a]	Sum of Square (SS)	df	Mean of Square (MS)	F-Test	*p*-Value [a]
Yield (%)	Linear	120.50	3	40.17	107.11	$\mathbf{2.8 \times 10^{-4}}$
	TP	72.00	1	72.00	192.00	$\mathbf{1.6 \times 10^{-4}}$
	RT	8.00	1	8.00	21.33	$\mathbf{9.9 \times 10^{-3}}$
	IR	40.50	1	40.50	108.00	$\mathbf{4.8 \times 10^{-3}}$
R^2 = 98.77%						
S_{BET} (m^2 g^{-1})	Linear	201,984	3	67,328	3.07	1.5×10^{-1}
	TP	1953	1	1953	0.09	7.8×10^{-1}
	RT	3	1	3	0.00	9.9×10^{-1}
	IR	200,028	1	200,028	9.11	$\mathbf{3.9 \times 10^{-2}}$
R^2 = 69.70%						
Adsorption MB (%) [b]	Linear	690.84	3	230.28	3.69	1.2×10^{-1}
	TP	16.13	1	16.13	0.26	6.4×10^{-1}
	RT	15.13	1	15.13	0.24	6.5×10^{-1}
	IR	659.59	1	659.59	10.57	$\mathbf{3.1 \times 10^{-2}}$
R^2 = 73.46%						
Adsorption AMX (%) [b]	Linear	17.4967	3	5.83	3.66	1.2×10^{-1}
	TP	1.4393	1	1.44	0.90	3.9×10^{-1}
	RT	0.1552	1	0.15	0.10	7.7×10^{-1}
	IR	15.9021	1	15.90	9.98	$\mathbf{3.4 \times 10^{-2}}$
R^2 = 73.29%						
Energy Consumption (Wh)	Linear	8,391,592	2	4,195,796	60.03	$\mathbf{3.2 \times 10^{-3}}$
	TP	1,397,792	1	1,397,792	20.00	$\mathbf{6.6 \times 10^{-3}}$
	RT	6,993,800	1	6,993,800	100.07	$\mathbf{1.7 \times 10^{-4}}$
R^2 = 96.00%						

Notes: TP—pyrolysis temperature (500 °C (−) and 700 °C (+)); RT—residence time (60 min (−) and 180 min (+)); IR—precursor:activating agent ratio (1:1 (−) and 1:2 (+)); R^2—a measure of the amount of variation around the mean explained by the model. [a] the bold *p*-value represents significant factors. [b] Experimental conditions: 100 mg L^{-1} MB and AMX solution, material dose of 1 g L^{-1}.

By using the coefficients assigned to each variable (TP, RT, and IR), the mathematical model was identified that most accurately represents the influence of the experimental parameters on the responses of the produced ACs. The S_{BET} value and adsorption percentages of MB and AMX were significantly influenced by IR, whereas TP and RT did not have a significant impact on these responses. Therefore, TP and RT were not included in the equations. Thus, the yield, S_{BET}, adsorption (%) of MB and AMX, and energy consumption can be expressed using Equations (10)–(14), respectively. The increase in positive values in each variable is directly related to the increase in each corresponding response. On the other hand, negative coefficients indicate an inverse effect on the response.

$$\text{Yield (\%)} = 40.75 - 6.000\,(\text{TP}) - 2.000\,(\text{RT}) - 4.500\,(\text{IR}) \quad (10)$$

$$S_{BET}\ (m^2\ g^{-1}) = 611.0 + 316.3\,(\text{IR}) \quad (11)$$

$$\text{MB adsorption (\%)} = 57.50 + 18.16\,(\text{IR}) \quad (12)$$

$$\text{AMX adsorption (\%)} = 92.31 + 2.820\,(\text{IR}) \quad (13)$$

$$\text{Energy consumption (Wh)} = -2189 + 836\,(\text{TP}) + 1870\,(\text{RT}) \quad (14)$$

Table 2 indicates that the three factors (TP, RT, and IR) influenced the yield of the ACs (*p*-value $\leq$ 0.05). Equation (10) highlights the pyrolysis temperature as the most relevant factor in the AC yield (due to the highest coefficient (6.000)), followed by the precursor:activating agent ratio and the residence time. As expected, the factors at low levels are favorable for increasing the AC yields. On the other hand, the factors at high levels decrease the yield, as shown in Figure 1a.

Table 2 shows the ratio of activating agent (IR) as the unique factor that affected the adsorption (%) of the materials. It is known that there is a direct relationship between the physical adsorption capacity and S_{BET}. Generally, higher S_{BET} improves the adsorptive performance of the materials, due to the larger pore volume. It is noted that higher S_{BET} were obtained using higher ratios of activating agent. These results are in line with Yakout and El-Deen (2016), who investigated the preparation of AC from olive stones at concentrations of 60, 70, and 80% of H_3PO_4. A higher S_{BET} (1218 m^2 g^{-1}) for the 80% H_3PO_4 concentration was obtained, while for 70 and 60%, the S_{BET} was 779 and 257 m^2 g^{-1}, respectively [60].

The main effect plots for yield, S_{BET}, adsorption of MB and AMX, and energy consumption are shown in Figure S1. The lines presented in the graphs indicate whether the factor has a negative or positive effect on the response, and which one has the greatest influence on a given response [61]. It is worth highlighting that the length of the line corresponds to the degree of statistical significance, with longer lines indicating greater importance of the factor in influencing the response variable.

The S_{BET} was assigned a weight of 1, while a weight of 0.5 was used for the other responses, namely, yield, adsorption capacity, and energy consumption. Emphasis was placed on maximizing yield, S_{BET}, and adsorption capacity, with the goal of minimizing the energy consumption. From the results presented, $AC_{700\text{-}60\text{-}1:2}$ was selected as the optimized material, produced at 700 °C (TP), residence time of 60 min (RT), and a precursor:activating ratio of 1:2 (IR). Table 3 shows the experimental, theoretical, and desirability function values for each response, for $AC_{700\text{-}60\text{-}1:2}$. According to the results presented, there is a close agreement between the theoretically calculated values (using Equations (10)–(14)) and the experimentally observed values, which indicates an effective optimization. The associated desirability value was 0.7490.

Table 3. Experimental, theoretical, and desirability function values of the responses for the $AC_{700\text{-}60\text{-}1:2}$ sample.

Responses	Priority	Experimental	Theoretical	Desirability
Yield	Maximize	18%	17.8%	0.36690 *
S_{BET}	Maximize	1335 m^2 g^{-1}	1244 m^2 g^{-1}	0.84402
MB adsorption	Maximize	98%	94%	0.92680 *
AMX adsorption	Maximize	99%	98%	0.93689 *
Energy consumption	Minimize	1144 Wh	1353 Wh	0.87652 *
Compound **				0.7490

Notes: * considering response weight 0.5. ** compound—desirability value considering all responses simultaneously. (Conditions MB and AMX adsorption: 100 mg L^{-1} solution, material dose of 1 g L^{-1}).

3.3. Characterization of the Optimized Activated Carbon

Figure 2 shows SEM-FEG, elemental analysis, and EDS obtained for the optimized AC ($AC_{700\text{-}60\text{-}1:2}$). The morphology of the $AC_{700\text{-}60\text{-}1:2}$ was obtained by SEM-FEG with different magnifications to find a more accurate morphological description, as depicted in Figure 2. The macro-surface of $AC_{700\text{-}60\text{-}1:2}$ obtained at a lower magnification (1000×) (Figure 2a) shows smooth plate-like structures of different sizes. By increasing the magnification by 20 times (20,000×), it is possible to observe the roughness of $AC_{700\text{-}60\text{-}1:2}$ (Figure 2b), and by 200 times (200,000×), the SEM-FEG images show the presence of several interconnected pores in the mesoporous region (2–50 nm) (Figure 2c).

The results from the EDS analysis show carbon (C), oxygen (O), phosphorus (P), and sulfur (S) elements on the surface of $AC_{700\text{-}60\text{-}1:2}$ (Figure 2d,i). In addition, the data obtained allowed the semi-quantitative analysis of these elements, and the content (expressed in mass (%)) obtained for C, O, P, and S were 88.9, 8.7, 1.8, and 0.6%, respectively. As expected, $AC_{700\text{-}60\text{-}1:2}$ is mainly composed of carbon, followed by oxygen. The presence of sulfur is due to the reagents used in the Kraft process [62]. As for phosphorus, and despite the washing procedures applied to $AC_{700\text{-}60\text{-}1:2}$, the residual levels obtained can be explained by

the chemical activation with H_3PO_4 and the incorporation of phosphate in the carbonaceous matrix through C-O-P [16]. As reported in the literature, a higher percentage of oxygen may be desirable for adsorbent materials because the presence of this element favors intermolecular interactions [63]. The elemental mapping (Figure 2e–h) shows that elements are homogeneously dispersed on the sample surface, indicating the chemical homogeneity of $AC_{700\text{-}60\text{-}1:2}$.

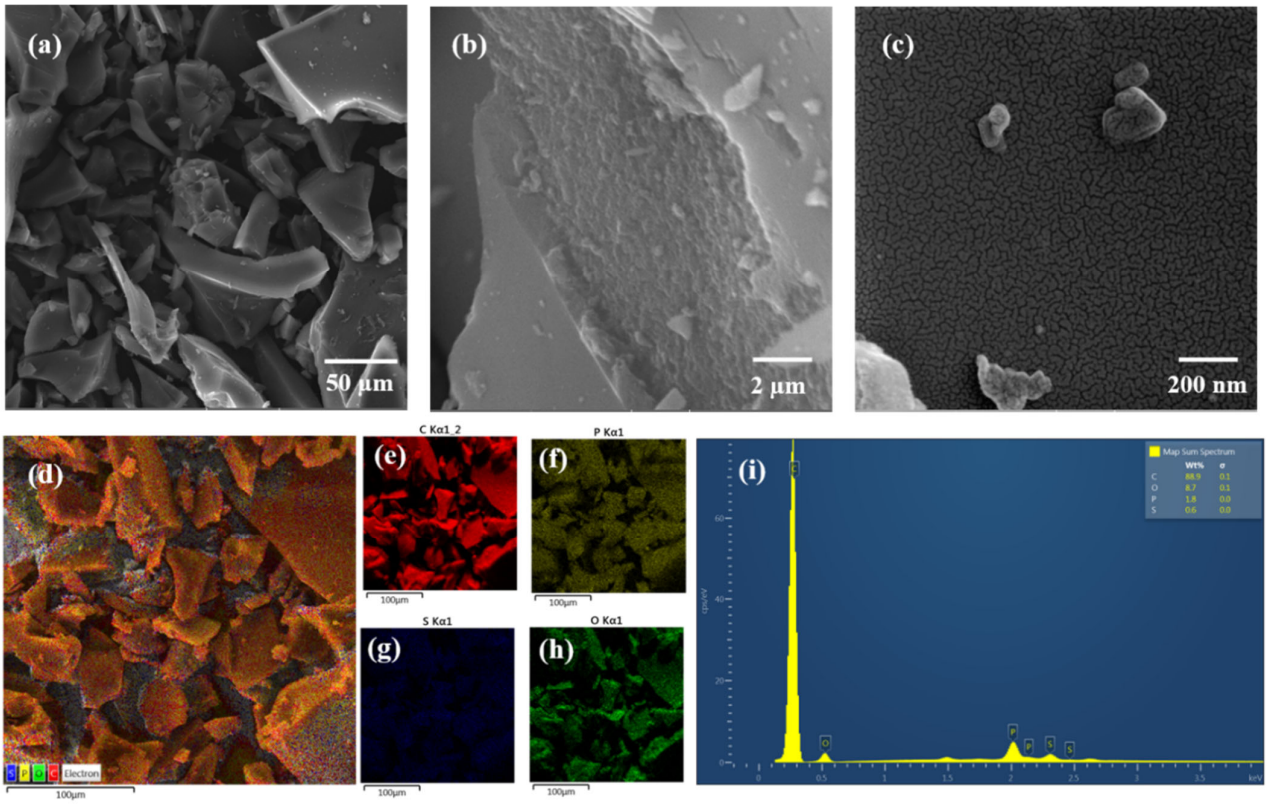


Figure 2. SEM-FEG of sample $AC_{700\text{-}60\text{-}1:2}$ at 1000 (**a**), 20,000 (**b**), and 200,000 (**c**) times magnification. Elemental mapping of C, O, S, and P (**d**), carbon (**e**), phosphorus (**f**), sulfur (**g**), oxygen (**h**), and spectrum EDS (**i**).

$AC_{700\text{-}60\text{-}1:2}$ was further characterized, and its chemical structure was evaluated by FT-IR and Raman spectroscopy. Additionally, the thermal behavior of $AC_{700\text{-}60\text{-}1:2}$ was explored by TGA/DGT analysis, and its surface net charge was determined (Figure 3).

The presence of functional groups or specific bonds was evaluated by FT-IR analysis. The obtained spectrum, depicted in Figure 3a, shows a band positioned at 3400 cm^{-1} which can be identified as aromatic and aliphatic OH groups [64]. The band at 2925 cm^{-1}, attributed to the stretching of the C-H group, is almost imperceptible, correlated with an adequate conversion of the precursor into AC [65]. The band at 1600 cm^{-1} refers to C=C vibrations in benzenic rings. Absorption close to 1440 cm^{-1} indicates the presence of methyl and methylene groups. The band between 1000 and 1300 cm^{-1} is related to P=O stretching, O-C vibrations of the P-O-C (aromatic) bond, or P=OOH [66,67]. It is worth mentioning that the studied lignin was chemically activated with H_3PO_4; as a consequence, the band in the region 1000 and 1300 cm^{-1} is attributed to the C-O stretching observed in alcohols, acids, ethers, phenols, and esters [68].

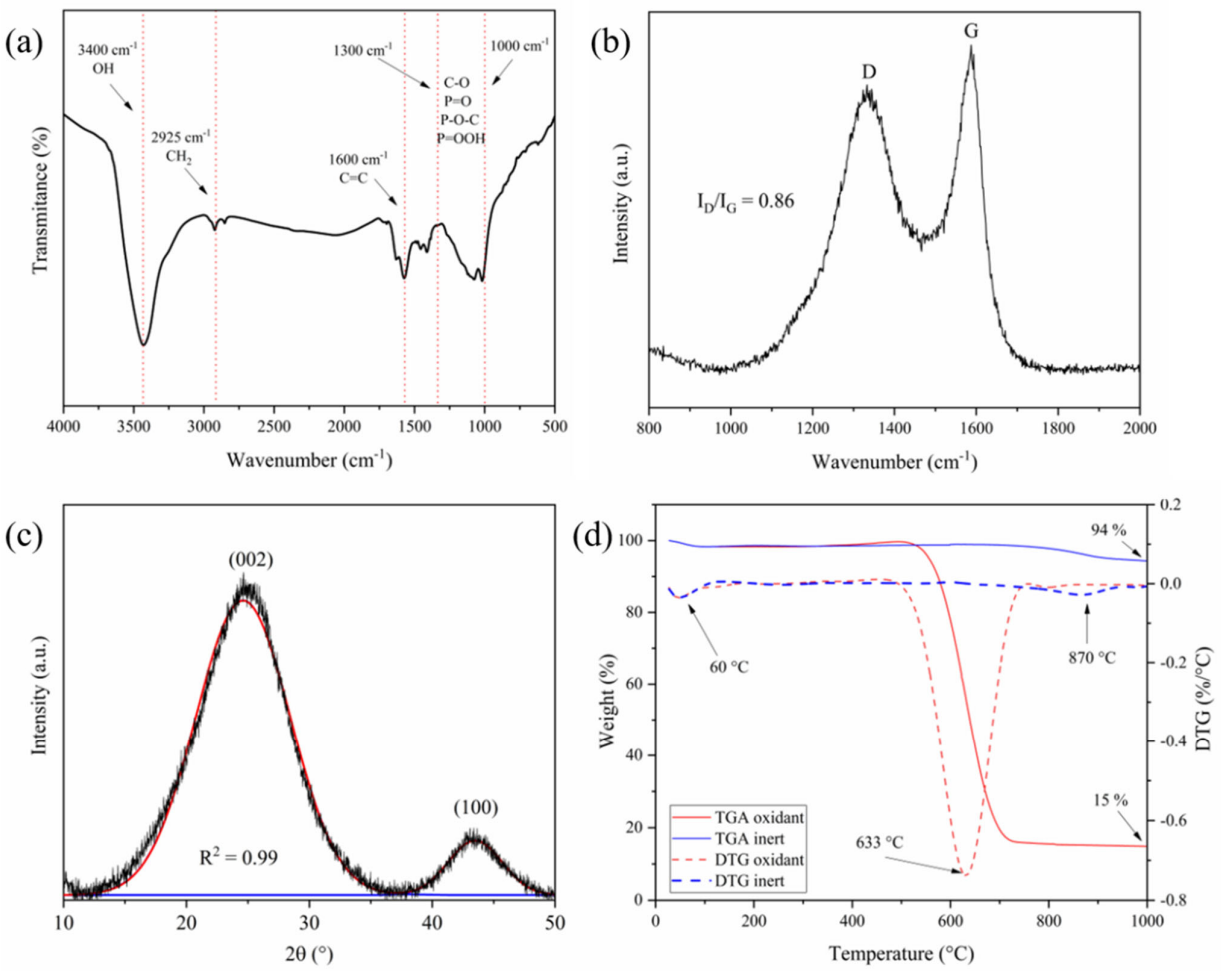


Figure 3. FT-IR (**a**), Raman (**b**), XRD (**c**), and TGA (**d**) of the optimized AC ($AC_{700\text{-}60\text{-}1:2}$).

$AC_{700\text{-}60\text{-}1:2}$ was analyzed by Raman spectroscopy and the spectrum (Figure 3b) revealed the presence of two broad bands. The first band, located at 1350 cm^{-1}, is known as the D-band and is indicative of graphitic structure with defects and the presence of sp^3 bonds [67]. The intensity of the D-band increases as the degree of defects in the graphitic structure increases. This band is attributed to the vibration mode of the A_{1G} symmetry [69]. The second band at 1580 cm^{-1} (G-band) is characteristic of an undisturbed structure (vibrational mode E_{2G}), related to the ordered graphitic structure [70]. The ratio of I_D/I_G intensities was 0.86; similar results were reported in the literature [67,68,71]. Comparatively, findings from a previous study indicated a higher I_D/I_G ratio (1.01) for the AC obtained in comparable conditions but in an air atmosphere [34]. This result indicates that the oxidizing atmosphere contributes to a decrease in structural ordering in comparison to the nitrogen atmosphere here applied.

Concerning XRD analysis, two broad and diffuse bands can be seen in Figure 3c, centered at 23° and 43°, due to reflections from the (002) and (100) planes. These bands are typical of carbon materials. This result indicates an amorphous structure with the presence of graphitic microcrystallites, also known as a turbostratic carbon structure [72]. The interplanar distance (d_{002}), the crystallite height (*Lc*), and crystallite width (*La*) were 0.36, 0.91, and 3.81 nm, respectively. Although there is no significant difference in the interplanar distance (d_{002}) for the material here described and materials produced under synthetic air atmosphere with the same precursor [34], a notable difference is observed in the crystallite width (*La*), which is lower in the synthetic air atmosphere. Overall, the results of Raman spectroscopy are consistent with the XRD results. This correlation confirms that the crystallographic ordering of produced carbonaceous materials was influenced by the

atmosphere used in the process, indicating that pyrolysis using a nitrogen atmosphere favored the attainment of better-ordered ACs. This outcome appears contradictory to the N_2 adsorption and desorption analysis, as it is the sample with the largest S_{BET}. This trend may be attributed to the likely rearrangement of carbonaceous structures, leading to increased microporosity, coupled with a decrease in larger voids.

Figure 3d shows the thermal behavior based on TGA/DTG analyses of $AC_{700\text{-}60\text{-}1:2}$ when heated from 25 to 1000 °C in oxidizing and inert atmospheres. In the range from 25 to 100 °C, the observed mass loss, in both atmospheres, is due to the release of low molar mass molecules and water. As the sample was previously dried in an oven, only a small mass loss is observed below 100 °C (>5%) and this is due to the water loss adsorbed during storage or handling of the sample. In an oxidizing atmosphere, the sample presents an accentuated weight in the range of 500 and 700 °C. After this temperature, a plateau is observed, and a final residue of 15% was obtained. This residue is due to the ash in the sample, as a result of the impregnation with H_3PO_4 and the Kraft process used to extract the cellulose. As shown in the DTG curve, the main peak is at 633 °C. In the oxidizing atmosphere, the sample presents thermal stability up to 500 °C, then the material starts to degrade.

In the inert atmosphere, the sample shows a weight loss of 6% ranging from 750 to 1000 °C, with the main peak centered at 870 °C. It is known that at this temperature range, the sample is decomposed releasing phenol, carbonyl, and hydroxyl groups [73,74]. The fixed carbon content of $AC_{700\text{-}60\text{-}1:2}$ was 79%, obtained by the difference between the residue content in an inert atmosphere and those determined under an oxidizing atmosphere. In contrast, the results obtained for AC synthesized in a synthetic air atmosphere [34] exhibited a lower fixed carbon content of 62%. Specifically, the higher fixed carbon content observed in the AC processed in an inert atmosphere suggests a higher carbon yield and fewer functional groups compared to the AC synthesized in a synthetic air atmosphere. This phenomenon can be attributed to the preferential formation of functional groups under synthetic air conditions, which subsequently lead to reduced stability of the carbon material. The presence of these functional groups renders a carbon material less stable, as they decompose before the carbon structure, ultimately impacting the overall stability and composition of the carbon material produced under different atmospheric conditions.

The PZC of $AC_{700\text{-}60\text{-}1:2}$ was 5, which indicates the slightly acidic nature of the surface. As the surface charge of AC depends on the pH of the solution and its PZC, for aqueous solutions with pH below the PZC, the surface of the sample should be mostly positively charged. On the other hand, for pH above the PZC, the sample surface is predominantly negative. Therefore, $AC_{700\text{-}60\text{-}1:2}$ is negatively charged at the pH of the aqueous solutions (pH 6–7) studied in this work. In this sense, it is expected to be a suitable adsorbent for positively charged contaminants, such as MB dye [75].

When considering AMX with different pKa values (pK_{a1} = 2.26, pK_{a2} = 7.49, and pK_{a3} = 9.63), it is important to note that the adsorbate may present different behavior, depending on the pH of the solution [76]. For example, at pH values above its first pKa, as is the case of the pH of the studied systems, AMX is predominantly in its neutral and negative forms, and its adsorption to the surface of sample $AC_{700\text{-}60\text{-}1:2}$ would be reduced due to non-favorable electrostatic interactions.

3.4. Kinetic Adsorption Experiments

The adsorptive performance of $AC_{700\text{-}60\text{-}1:2}$ in removing the MB cationic dye and the AMX antibiotic from aqueous media was investigated in the present work. Figure 4a,b show the experimental kinetic curves (q_t vs. t) of the adsorption of MB and AMX on $AC_{700\text{-}60\text{-}1:2}$ and the corresponding fittings. The fitted parameters for each system, using pseudo-first-order, pseudo-second-order, and Elovich non-linear models, are listed in Table 4.

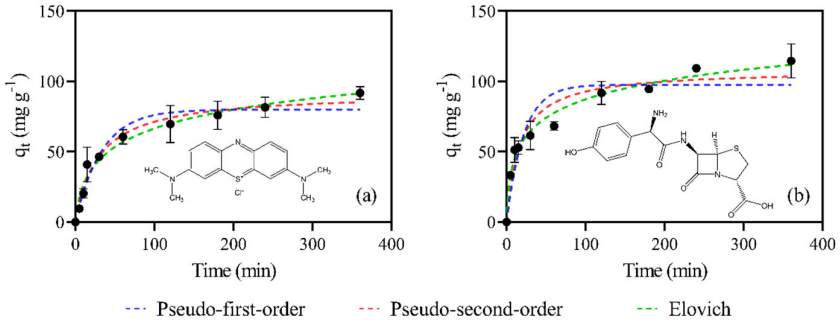


Figure 4. Kinetic modeling of the experimental results on the adsorption of MB (**a**) and AMX (**b**) using pseudo-first-order, pseudo-second-order, and Elovich models. (Conditions: 400 mg L^{-1} solution, material dose of 1 g L^{-1}, 120 rpm for 24 h, at room temperature). The error bars correspond to standard deviation (n = 3).

Table 4. Fit parameters of the pseudo-first-order, pseudo-second-order, and Elovich models for MB and AMX adsorption on the optimized material ($AC_{700\text{-}60\text{-}1:2}$).

		Contaminants	
Kinetic Model		**MB**	**AMX**
pseudo-first-order	k_1 (min^{-1})	0.030 ± 0.005	0.05 ± 0.01
	q_e (mg g^{-1})	80 ± 4	98 ± 7
	R^2	0.95	0.87
	$S_{y/x}$	7.13	13.96
pseudo-second-order	k_2 (g mg^{-1} min^{-1})	0.0004 ± 0.0007	0.0006 ± 0.0001
	q_e (mg g^{-1})	92 ± 4	108 ± 6
	R^2	0.98	0.94
	$S_{y/x}$	4.95	9.62
Elovich	α (mg g^{-1} min^{-1})	5 ± 1	18 ± 4
	β (mg g^{-1})	0.050 ± 0.004	0.052 ± 0.003
	R^2	0.98	0.98
	$S_{y/x}$	4.92	4.89

Notes: k_1: pseudo-first-order rate constant; k_2: pseudo-second-order rate constant; q_e: adsorption amount at equilibrium; α: initial adsorption rate; β: desorption constant; R^2: determination coefficient; $S_{y/x}$: error.

As can be observed in Figure 4a,b the q_t values sharply increased in the initial phase (up to t~60 min), which represents a rapid adsorption of MB and AMX from the aqueous medium, and then proceeds at a slower rate until the equilibrium is reached. After 240 min, the equilibrium is reached, corresponding to MB and AMX removal of 77 and 73%, respectively, for the studied material dose. Table 4 presents the estimated parameters of the fitted kinetic models. The adsorption data for $AC_{700\text{-}60\text{-}1:2}$ show a better fit to the Elovich model, with R^2 values of 0.98 for both MB and AMX. This adsorption model considers chemisorption between adsorbent and adsorbate [77].

3.5. Equilibrium Adsorption Experiments

The experimental equilibrium data were evaluated using the Langmuir and Freundlich isotherm models, as shown in Figure 5a,b. Table 5 presents the model parameters and determination coefficients (R^2). The analysis of these data shows that the adsorption of MB on $AC_{700\text{-}60\text{-}1:2}$ is better described by the Freundlich isotherm, with R^2 equal to 0.98. For the adsorption of AMX, the R^2 was 0.97 for both the Langmuir and Freundlich models. It is important to highlight that the Freundlich isotherm describes the adsorption taking place in multiple layers, involving interactions between the adsorbed molecules, being particularly suitable for heterogeneous systems [78], while the Langmuir model assumes monolayer adsorption.

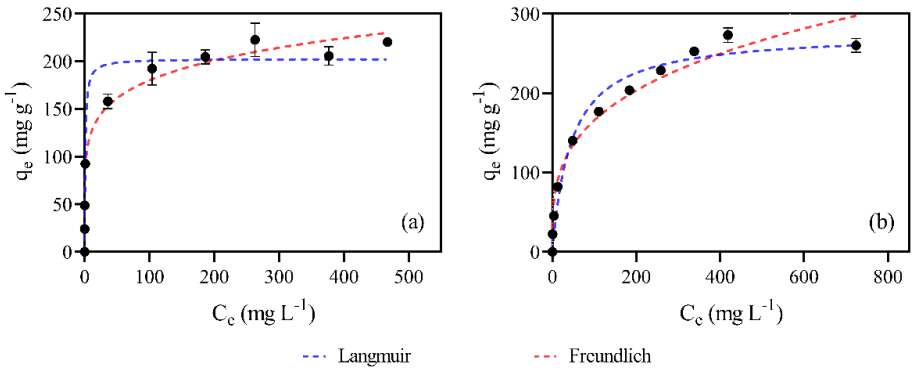


Figure 5. Equilibrium experimental data and fittings to Langmuir and Freundlich models for MB (**a**) and AMX (**b**). (Conditions: material dose of 1 g L^{-1}, 120 rpm for 24 h at room temperature). The error bars correspond to standard deviation (n = 3).

Table 5. Isothermal parameters of Langmuir and Freundlich models for MB and AMX adsorption on the produced $AC_{700\text{-}60\text{-}1:2}$.

		Contaminants	
		MB	**AMX**
Langmuir	q_m (mg g^{-1})	203 ± 8	276 ± 14
	K_L (L mg^{-1})	1.0 ± 0.3	0.022 ± 0.005
	R^2	0.96	0.97
	$S_{y/x}$	19.68	17.61
Freundlich	K_F (mg g^{-1}(mg L^{-1})$^{1/n}$)	87 ± 9	42 ± 7
	n_F	6.3 ± 0.7	3.4 ± 0.3
	R^2	0.98	0.97
	$S_{y/x}$	14.74	17.82

Notes: q_m: adsorption capacity; K_L: Langmuir constant; K_F: Freundlich constant; n_F: adsorption intensity; R^2: determination coefficient, $S_{y/x}$: error.

The experimental q_m values were 210 mg g^{-1} for MB and 280 mg g^{-1} for AMX, respectively. The obtained Langmuir q_m values were close to the experimental values, further supporting the adequacy of this model to describe the data. Kraft lignin AC obtained in a synthetic air atmosphere in a previous study [34] revealed a much lower adsorption capacity of 80 mg g^{-1} for MB, obtained under comparable experimental adsorption conditions (no data for AMX are available for comparison), highlighting the importance of the atmosphere used in the materials production on their adsorptive performance.

3.6. Comparison with Literature Studies and Future Work

According to the literature, many researchers have investigated the preparation and application of ACs from various biomass sources. Table 6 displays a comparison of the S_{BET} and q_m of MB and AMX for AC samples obtained from different precursors.

As can be seen, for the S_{BET} values, AC from Kraft lignin shows higher values than for all AC obtained from different biomass sources and even than some commercial AC applied in this context and depicted in Table 6. This is an interesting finding, given that the AC produced in the present study used a lower temperature of pyrolysis (only 700 °C). Also, the q_m values obtained in this study were much higher or similar to the materials with the highest performance. Yet, it is noteworthy that comparison between different adsorption studies is always critical due to the lack of consistency in the experimental parameters that largely influence the adsorption process, such as contaminant concentration, material dose, and pH.

Table 6. Specific surface area and maximum adsorption capacity of AC samples from different origins for the removal of MB and AMX from water.

Activated Carbon	Organic Pollutant	Activator	S_{BET} (m^2 g^{-1})	Experimental Conditions			q_m (mg g^{-1})	Reference
				Adsorbent Dose (g L^{-1})	Concentration (mg L^{-1})	pH		
Kraft lignin	MB	H_3PO_4	1150	1	25–1000		80	[34]
Spathodea campanulata		H_3PO_4	1054	2	90	9	90	[29]
Cardboard tube		H_3PO_4	468.9	6.4	50–1000	6	182.5	[79]
Corn Cob		KOH	492	0.8	100–500	-	333	[80]
Papaya peels		H_3PO_4		3	10	6	46.9	[81]
Coffee husk		H_2SO_4	0.98	5	100–500	8	88.1	[82]
Sugarcane bagasse waste		KOH	709.3	0.8	50–250	8	136.5	[30]
Doum fibers		H_3PO_4		1	30	6	83.3	[83]
Lignin		H_3PO_4	1035	1	25–700		151.5	[65]
Kraft lignin ($AC_{700\text{-}60\text{-}1:2}$)		H_3PO_4	1335	1	25–1000		210	This study
Paper mill sludge	AMX	KOH	1196	0.0125–0.05	5		204	[39]
Aloe vera leaves		H_2SO_4	412	2	10–50	3	28.8	[84]
Tecoma chip wood		KOH/CO_2	924.8	1	25–300		357.1	[85]
Date pits		CO_2	1325	1	20–700		424.3	[32]
AC commercial			1100	1	20–700		313.7	[32]
Pomegranate peel		H_3PO_4		1.5	10	5	40.2	[86]
Olive biomass		$ZnCl_2$	1742	1.5	400	7	237	[87]
Reed		H_3PO_4	880.5	1	10–60		76.3	[88]
AC commercial			462.9	12.5	10–1000		4.4	[31]
Kraft lignin ($AC_{700\text{-}60\text{-}1:2}$)		H_3PO_4	1335	1	25–1000		280	This study

Overall, the AC produced in this study under optimal conditions demonstrated high efficiency as an adsorbent for both MB and AMX. These results inspire additional research, which could encompass exploring different pH in adsorption studies, understanding the adsorption mechanisms, investigating reusability, and evaluating the effectiveness of AC in real environmental conditions.

4. Conclusions

An industrial residue of Kraft lignin was successfully converted into activated carbon (AC), with further application in the removal of a dye (MB) and an antibiotic (AMX) from water. The production of AC from Kraft lignin was conducted according to a full factorial design (2^3) for the optimization of specific surface area (S_{BET}), yield (%), energy consumption (Wh), and adsorptive removal of MB and AMX from water. The obtained results evidenced that the yield was negatively influenced by increasing pyrolysis temperature (700 °C) and activating agent:precursor ratio (1:2). The same activating agent:precursor ratio significantly maximized the S_{BET} and the adsorptive removal responses for both contaminants. The optimal production conditions were determined to be pyrolysis at 700 °C for 60 min with a precursor:activating agent ratio of 1:2, as determined by desirability function, originating the material $AC_{700\text{-}60\text{-}1:2}$. Batch kinetic and equilibrium adsorption experiments were accomplished for the optimized $AC_{700\text{-}60\text{-}1:2}$, revealing a maximum adsorption capacity of 210 mg g^{-1} for MB and 280 mg g^{-1} for AMX, with equilibrium being reached within 240 min for both contaminants. Comparison with previous work revealed that nitrogen atmosphere during pyrolysis favors higher S_{BET} and adsorption capacities compared to synthetic air atmosphere.

Supplementary Materials: The following supporting information can be downloaded at: https://www.mdpi.com/article/10.3390/w16131838/s1, Figure S1: Main effects plot for yield (a), S_{BET} (b), MB adsorption (c), AMX adsorption (d), and energy consumption (e). Table S1: Chemical information about methylene blue (MB) and amoxicillin (AMX); Table S2: Experimental conditions of experiments and responses obtained for the ACs samples.

Author Contributions: T.R.B.: conceptualization, methodology, validation, formal analysis, investigation, writing—original draft; É.M.L.S.: formal analysis, investigation, writing—original draft; E.G.R.d.A.: writing—review and editing; N.K.M.: writing—review and editing; L.S.R.: conceptualization, methodology, formal analysis, investigation, supervision; M.G.: formal analysis, writing—review and editing; V.C.: conceptualization, methodology, formal analysis, investigation, resources, writing—review and editing, supervision; M.C.R.: writing—review and editing, supervision. All authors have read and agreed to the published version of the manuscript.

Funding: This study was partially financed by the Brazilian Funding Institutions Coordenação de Aperfeiçoamento de Pessoal de Nível Superior—Brasil (CAPES)—Finance Code 001 and CNPq (Conselho Nacional de Desenvolvimento Científico e Tecnológico) (305123/2018-1). The authors are also grateful to Divisão de Química/Instituto de Aeronáutica e Espaço, Fibria Celulose S.A. Co. supplying lignin. The authors also acknowledge financial support to CESAM by FCT/MCTES (UIDP/50017/2020+UIDB/50017/2020+LA/P/0094/2020), through national funds. Érika M.L. Sousa thanks Fundação para a Ciência e Tecnologia (FCT) for her Ph.D. grant (2020.05390.BD).

Data Availability Statement: Data is contained within the article.

Conflicts of Interest: The authors declare that they have no known competing financial interests or personal relationships that could have appeared to influence the work reported in this paper.

References

1. Idris, R.; Chong, W.W.F.; Ali, A.; Idris, S.; Hasan, M.F.; Ani, F.N.; Chong, C.T. Phenol-Rich Bio-Oil Derivation via Microwave-Induced Fast Pyrolysis of Oil Palm Empty Fruit Bunch with Activated Carbon. *Environ. Technol. Innov.* **2021**, *21*, 101291. [CrossRef]
2. Tripathi, M.; Sahu, J.N.; Ganesan, P. Effect of Process Parameters on Production of Biochar from Biomass Waste through Pyrolysis: A Review. *Renew. Sustain. Energy Rev.* **2016**, *55*, 467–481. [CrossRef]
3. Hu, Z.; Ma, X.; Chen, C. A Study on Experimental Characteristic of Microwave-Assisted Pyrolysis of Microalgae. *Bioresour. Technol.* **2012**, *107*, 487–493. [CrossRef] [PubMed]
4. Vargas-Moreno, J.M.; Callejón-Ferre, A.J.; Pérez-Alonso, J.; Velázquez-Martí, B. A Review of the Mathematical Models for Predicting the Heating Value of Biomass Materials. *Renew. Sustain. Energy Rev.* **2012**, *16*, 3065–3083. [CrossRef]
5. Ragauskas, A.J.; Beckham, G.T.; Biddy, M.J.; Chandra, R.; Chen, F.; Davis, M.F.; Davison, B.H.; Dixon, R.A.; Gilna, P.; Keller, M.; et al. Lignin Valorization: Improving Lignin Processing in the Biorefinery. *Science* **2014**, *344*, 1246843. [CrossRef] [PubMed]
6. Wang, H.; Pu, Y.; Ragauskas, A.; Yang, B. Bioresource Technology from Lignin to Valuable Products—Strategies, Challenges, and Prospects. *Bioresour. Technol.* **2019**, *271*, 449–461. [CrossRef] [PubMed]
7. Sarkanen, K.V.; Ludwig, C.H. *Lignins Occurence, Formation, Structure and Reactions*; John Wiley: New York, NY, USA, 1971.
8. Huang, J.; Fu, S.; Gan, L. *Lignin Chemistry and Applications*; Elsevier: Alpharetta, GA, USA, 2018; ISBN 9788578110796.
9. Wan, X.; Shen, F.; Hu, J.; Huang, M.; Zhao, L.; Zeng, Y.; Tian, D.; Yang, G.; Zhang, Y. 3-D Hierarchical Porous Carbon from Oxidized Lignin by One-Step Activation for High-Performance Supercapacitor. *Int. J. Biol. Macromol.* **2021**, *180*, 51–60. [CrossRef]
10. Anderson, E.M.; Stone, M.L.; Katahira, R.; Reed, M.; Beckham, G.T.; Román-Leshkov, Y. Flowthrough Reductive Catalytic Fractionation of Biomass. *Joule* **2017**, *1*, 613–622. [CrossRef]
11. Madhu, R.; Periasamy, A.P.; Schlee, P.; Hérou, S.; Titirici, M.M. Lignin: A Sustainable Precursor for Nanostructured Carbon Materials for Supercapacitors. *Carbon. N. Y.* **2023**, *207*, 172–197. [CrossRef]
12. Chen, M.; Li, Y.; Liu, H.; Zhang, D.; Shi, Q.S.; Zhong, X.Q.; Guo, Y.; Xie, X.B. High Value Valorization of Lignin as Environmental Benign Antimicrobial. *Mater. Today Bio* **2023**, *18*, 100520. [CrossRef]
13. Supanchaiyamat, N.; Jetsrisuparb, K.; Knijnenburg, J.T.N.; Tsang, D.C.W.; Hunt, A.J. Lignin Materials for Adsorption: Current Trend, Perspectives and Opportunities. *Bioresour. Technol.* **2019**, *272*, 570–581. [CrossRef] [PubMed]
14. Mohamed, A.R.; Mohammadi, M.; Darzi, G.N. Preparation of Carbon Molecular Sieve from Lignocellulosic Biomass: A Review. *Renew. Sustain. Energy Rev.* **2010**, *14*, 1591–1599. [CrossRef]
15. Lora, J.H.; Glasser, W.G. Recent Industrial Applications of Lignin: A Sustainable Alternative to Nonrenewable Materials. *J. Polym. Environ.* **2002**, *10*, 39–48. [CrossRef]
16. Liou, T.H. Development of Mesoporous Structure and High Adsorption Capacity of Biomass-Based Activated Carbon by Phosphoric Acid and Zinc Chloride Activation. *Chem. Eng. J.* **2010**, *158*, 129–142. [CrossRef]
17. Jonathan, Y.C. *Activated Carbon. Fiber and Textiles*; Elsevier: Alpharetta, GA, USA, 2017; ISBN 9780081009079.
18. Marsh, H.; Rodríguez-Reinoso, F. *Characterization of Activated Carbon*; Elsevier Science & Technology Books: Alpharetta, GA, USA, 2006; ISBN 0080444636.
19. Azmi, N.Z.M.; Buthiyappan, A.; Raman, A.A.A.; Patah, M.F.A.; Sufian, S. Recent Advances in Biomass Based Activated Carbon for Carbon Dioxide Capture—A Review. *J. Ind. Eng. Chem.* **2022**, *116*, 1–20. [CrossRef]

20. Afshin, S.; Rashtbari, Y.; Vosough, M.; Dargahi, A.; Fazlzadeh, M.; Behzad, A.; Yousefi, M. Application of Box–Behnken Design for Optimizing Parameters of Hexavalent Chromium Removal from Aqueous Solutions Using Fe_3O_4 Loaded on Activated Carbon Prepared from Alga: Kinetics and Equilibrium Study. *J. Water Process Eng.* **2021**, *42*, 102113. [CrossRef]
21. Brazil, T.R.; Gonçalves, M.; Anjos, E.G.R.; Junior, M.S.O.; Rezende, M.C. Microwave—Assisted Production of Activated Carbon in an Adapted Domestic Oven from Lignocellulosic Waste. *Biomass Convers. Biorefinery* **2021**, *14*, 255–268. [CrossRef]
22. Canales-Flores, R.A.; Prieto-García, F. Taguchi Optimization for Production of Activated Carbon from Phosphoric Acid Impregnated Agricultural Waste by Microwave Heating for the Removal of Methylene Blue. *Diam. Relat. Mater.* **2020**, *109*, 108027. [CrossRef]
23. Oladoye, P.O.; Ajiboye, T.O.; Omotola, E.O.; Oyewola, O.J. Methylene Blue Dye: Toxicity and Potential Elimination Technology from Wastewater. *Results Eng.* **2022**, *16*, 100678. [CrossRef]
24. European Commission Decision (EU). 2020/1161 of 4 August 2020 Establishing a Watch List of SUBSTANCES for Union-Wide Monitoring in the Field of Water Policy Pursuant to Directive 2008/105/EC of the European Parliament and of the Council. Available online: https://eur-lex.europa.eu/eli/dec_impl/2020/1161/oj (accessed on 20 June 2024).
25. Lu, T.; Cao, W.; Liang, H.; Deng, Y.; Zhang, Y.; Zhu, M.; Ma, W.; Xiong, R.; Huang, C. Blow-Spun Nanofibrous Membrane for Simultaneous Treatment of Emulsified Oil/Water Mixtures, Dyes, and Bacteria. *Langmuir* **2022**, *38*, 15729–15739. [CrossRef]
26. Liu, Z.; Sun, D.; Wang, C.; You, B.; Li, B.; Han, J.; Jiang, S.; Zhang, C.; He, S. Zeolitic Imidazolate Framework-67 and Its Derivatives for Photocatalytic Applications. *Coord. Chem. Rev.* **2024**, *502*, 215612. [CrossRef]
27. Portela, C.I.; Brazil, T.R.; Mendonça, T.A.P.; Santos, E.B.; Domingues, R.A.; Vieira, N.C.S.; Gonçalves, M. Activated Carbon Obtained from Coffee Husk Waste Activated by $CaCl_2$ as Support of TiO_2 for the Enhanced Photocatalytic Degradation of Victoria Blue B Dye. *Diam. Relat. Mater.* **2023**, *139*, 110417. [CrossRef]
28. Kumar, N.; Pandey, A.; Rosy; Sharma, Y.C. A Review on Sustainable Mesoporous Activated Carbon as Adsorbent for Efficient Removal of Hazardous Dyes from Industrial Wastewater. *J. Water Process Eng.* **2023**, *54*, 104054. [CrossRef]
29. Dimbo, D.; Abewaa, M.; Adino, E.; Mengistu, A.; Takele, T.; Oro, A.; Rangaraju, M. Methylene Blue Adsorption from Aqueous Solution Using Activated Carbon of Spathodea Campanulata. *Results Eng.* **2024**, *21*, 101910. [CrossRef]
30. Jawad, A.H.; Abdulhameed, A.S.; Bahrudin, N.N.; Hum, N.N.M.F.; Surip, S.N.; Syed-Hassan, S.S.A.; Yousif, E.; Sabar, S. Microporous Activated Carbon Developed from KOH Activated Biomass Waste: Surface Mechanistic Study of Methylene Blue Dye Adsorption. *Water Sci. Technol.* **2021**, *84*, 1858–1872. [CrossRef]
31. de Franco, M.A.E.; de Carvalho, C.B.; Bonetto, M.M.; Soares, R.d.P.; Féris, L.A. Removal of Amoxicillin from Water by Adsorption onto Activated Carbon in Batch Process and Fixed Bed Column: Kinetics, Isotherms, Experimental Design and Breakthrough Curves Mod. *J. Clean. Prod.* **2017**, *161*, 947–956. [CrossRef]
32. Belhachemi, M.; Djelaila, S. Removal of Amoxicillin Antibiotic from Aqueous Solutions by Date Pits Activated Carbons. *Environ. Process.* **2017**, *4*, 549–561. [CrossRef]
33. Brazil, T.R.; Junior, M.S.O.; Baldan, M.R.; Massi, M.; Rezende, M.C. Effect of Different Superficial Treatments on Structural, Morphological and Superficial Area of Kraft Lignin Based Charcoal. *Vib. Spectrosc.* **2018**, *99*, 130–136. [CrossRef]
34. Brazil, T.R.; Gonçalves, M.; Junior, M.S.O.; Rezende, M.C. A Statistical Approach to Optimize the Activated Carbon Production from Kraft Lignin Based on Conventional and Microwave Processes. *Microporous Mesoporous Mater.* **2020**, *308*, 110485. [CrossRef]
35. Kriaa, A.; Hamdi, N.; Srasra, E. Removal of Cu (II) from Water Pollutant with Tunisian Activated Lignin Prepared by Phosphoric Acid Activation. *Desalination* **2010**, *250*, 179–187. [CrossRef]
36. Montané, D.; Torné-Fernández, V.; Fierro, V. Activated Carbons from Lignin: Kinetic Modeling of the Pyrolysis of Kraft Lignin Activated with Phosphoric Acid. *Chem. Eng. J.* **2005**, *106*, 1–12. [CrossRef]
37. Myglovets, M.; Poddubnaya, O.I.; Sevastyanova, O.; Lindström, M.E.; Gawdzik, B.; Sobiesiak, M.; Tsyba, M.M.; Sapsay, V.I.; Klymchuk, D.O.; Puziy, A.M. Preparation of Carbon Adsorbents from Lignosulfonate by Phosphoric Acid Activation for the Adsorption of Metal Ions. *Carbon. N. Y.* **2014**, *80*, 771–783. [CrossRef]
38. Zuo, S.; Yang, J.; Liu, J.; Cai, X. Significance of the Carbonization of Volatile Pyrolytic Products on the Properties of Activated Carbons from Phosphoric Acid Activation of Lignocellulosic Material. *Fuel Process. Technol.* **2009**, *90*, 994–1001. [CrossRef]
39. Sousa, É.; Rocha, L.; Jaria, G.; Gil, M.V.; Otero, M.; Esteves, V.I.; Calisto, V. Optimizing Microwave-Assisted Production of Waste-Based Activated Carbons for the Removal of Antibiotics from Water. *Sci. Total Environ.* **2021**, *752*, 141662. [CrossRef] [PubMed]
40. Jaria, G.; Silva, C.P.; Ferreira, C.I.A.; Otero, M.; Calisto, V. Sludge from Paper Mill Effluent Treatment as Raw Material to Produce Carbon Adsorbents: An Alternative Waste Management Strategy. *J. Environ. Manage* **2017**, *188*, 203–211. [CrossRef] [PubMed]
41. Sousa, É.M.L.; Otero, M.; Rocha, L.S.; Gil, M.V.; Ferreira, P.; Esteves, V.I.; Calisto, V. Multivariable Optimization of Activated Carbon Production from Microwave Pyrolysis of Brewery Wastes—Application in the Removal of Antibiotics from Water. *J. Hazard. Mater.* **2022**, *431*, 128556. [CrossRef]
42. Brunauer, S.; Emmett, P.H.; Teller, E. Adsorption of Gases in Multimolecular Layers. *J. Am. Chem. Soc.* **1938**, *60*, 309–319. [CrossRef]
43. Derringer, G.; Suich, R. Simultaneous Optimization of Several Response Variables. *J. Qual. Technol.* **1980**, *12*, 214–219. [CrossRef]
44. Callister, W.D. *Materials Science and Engineering—An Introduction*; LTC Edition: Rio Janeiro, Brazil, 2008.
45. Al-Degs, Y.S.; El-Barghouthi, M.I.; El-Sheikh, A.H.; Walker, G.M. Effect of Solution PH, Ionic Strength, and Temperature on Adsorption Behavior of Reactive Dyes on Activated Carbon. *Dye. Pigment.* **2008**, *77*, 16–23. [CrossRef]

46. Lagergren, S. About the Theory of So-Called Adsorption of Soluble Substances, Kungliga Svenska Vetenskapsakademiens. *Handl. Band.* **1898**, *24*, 1.
47. Aurich, A.; Hofmann, J.; Oltrogge, R.; Wecks, M.; Gläser, R.; Blömer, L.; Mauersberger, S.; Müller, R.A.; Sicker, D.; Giannis, A. Pseudo-Second Order Model for Sorption Processes. *Process Biochem.* **2017**, *34*, 451–465. [CrossRef]
48. Chien, S.H.; Clayton, W.R. Application of Elovich Equation to the Kinetics of Phosphate Release and Sorption in Soils. *Soil. Sci. Soc. Am. J.* **1980**, *44*, 265–268. [CrossRef]
49. Armbruster, M.H.; Austin, J.B. The Adsorption of Gases on Plane Surfaces of Mica. *J. Am. Chem. Soc.* **1938**, *60*, 467–475. [CrossRef]
50. Limousin, G.; Gaudet, J.P.; Charlet, L.; Szenknect, S.; Barthès, V.; Krimissa, M. Sorption Isotherms: A Review on Physical Bases, Modeling and Measurement. *Appl. Geochem.* **2007**, *22*, 249–275. [CrossRef]
51. Yorgun, S.; Yildiz, D. Preparation and Characterization of Activated Carbons from Paulownia Wood by Chemical Activation with H_3PO_4. *J. Taiwan. Inst. Chem. Eng.* **2015**, *53*, 122–131. [CrossRef]
52. Gueye, M.; Richardson, Y.; Kafack, F.T.; Blin, J. High Efficiency Activated Carbons from African Biomass Residues for the Removal of Chromium (VI) from Wastewater. *J. Environ. Chem. Eng.* **2014**, *2*, 273–281. [CrossRef]
53. Prahas, D.; Kartika, Y.; Indraswati, N.; Ismadji, S. Activated Carbon from Jackfruit Peel Waste by H_3PO_4 Chemical Activation: Pore Structure and Surface Chemistry Characterization. *Chem. Eng. J.* **2008**, *140*, 32–42. [CrossRef]
54. Thommes, M.; Kaneko, K.; Neimark, A.V.; Olivier, J.P.; Rodriguez-Reinoso, F.; Rouquerol, J.; Sing, K.S.W. Physisorption of Gases, with Special Reference to the Evaluation of Surface Area and Pore Size Distribution (IUPAC Technical Report). *Pure Appl. Chem.* **2015**, *87*, 1051–1069. [CrossRef]
55. Wang, X.; Cheng, H.; Ye, G.; Fan, J.; Yao, F.; Wang, Y.; Jiao, Y.; Zhu, W.; Huang, H.; Ye, D. Key Factors and Primary Modification Methods of Activated Carbon and Their Application in Adsorption of Carbon-Based Gases: A Review. *Chemosphere* **2022**, *287*, 131995. [CrossRef]
56. Luo, Z.; Yao, B.; Yang, X.; Wang, L.; Xu, Z.; Yan, X.; Tian, L.; Zhou, H.; Zhou, Y. Novel Insights into the Adsorption of Organic Contaminants by Biochar: A Review. *Chemosphere* **2022**, *287*, 132113. [CrossRef]
57. Ioannidou, O.; Zabaniotou, a. Agricultural Residues as Precursors for Activated Carbon Production—A Review. *Renew. Sustain. Energy Rev.* **2007**, *11*, 1966–2005. [CrossRef]
58. Suhas; Carrott, P.J.M.; Ribeiro Carrott, M.M.L. Lignin—From Natural Adsorbent to Activated Carbon: A Review. *Bioresour. Technol.* **2007**, *98*, 2301–2312. [CrossRef] [PubMed]
59. Harimisa, G.E.; Jusoh, N.W.C.; Tan, L.S.; Ghafar, N.A. Influence of Furnace Atmospheres and Potassium Hydroxide Activation on the Properties of Bamboo Activated Carbon and Its Adsorption towards 4-Nitrophenol. *Chem. Eng. Res. Des.* **2023**, *198*, 325–339. [CrossRef]
60. Yakout, S.M.; Sharaf El-Deen, G. Characterization of Activated Carbon Prepared by Phosphoric Acid Activation of Olive Stones. *Arab. J. Chem.* **2016**, *9*, S1155–S1162. [CrossRef]
61. Bingol, D.; Tekin, N.; Alkan, M. Brilliant Yellow Dye Adsorption onto Sepiolite Using a Full Factorial Design. *Appl. Clay Sci.* **2010**, *50*, 315–321. [CrossRef]
62. Chakar, F.S.; Ragauskas, A.J. Review of Current and Future Softwood Kraft Lignin Process Chemistry. *Ind. Crops Prod.* **2004**, *20*, 131–141. [CrossRef]
63. Yang, G.X.; Jiang, H. Amino Modification of Biochar for Enhanced Adsorption of Copper Ions from Synthetic Wastewater. *Water Res.* **2014**, *48*, 396–405. [CrossRef] [PubMed]
64. Supaluknari, S.; Larkins, F.P.; Redlich, P.; Jackson, W.R. An FTIR Study of Australian Coals: Characterization of Oxygen Functional Groups. *Fuel Process. Technol.* **1988**, *19*, 123–140. [CrossRef]
65. Brazil, T.R.; Gonçalves, M.; Junior, M.S.O.; Rezende, M.C. Sustainable Process to Produce Activated Carbon from Kraft Lignin Impregnated with H_3PO_4 Using Microwave Pyrolysis. *Biomass Bioenergy* **2022**, *156*, 106333. [CrossRef]
66. Puziy, A.M.; Poddubnaya, O.I.; Martínez-Alonso, A.; Castro-Muñiz, A.; Suárez-García, F.; Tascón, J.M.D. Oxygen and Phosphorus Enriched Carbons from Lignocellulosic Material. *Carbon. N. Y.* **2007**, *45*, 1941–1950. [CrossRef]
67. Yao, Y.; Ge, D.; Yu, Y.; Zhang, Y.; Du, C.; Ye, H.; Wan, L.; Chen, J.; Xie, M. Filling Macro/Mesoporosity of Commercial Activated Carbon Enables Superior Volumetric Supercapacitor Performances. *Microporous Mesoporous Mater.* **2023**, *350*, 112446. [CrossRef]
68. Shamsabadi, A.S.; Bazarganipour, M.; Tavanai, H. An Investigation on the Pore Characteristics of Dates Stone Based Microwave Activated Carbon Nanostructures. *Diam. Relat. Mater.* **2021**, *120*, 108662. [CrossRef]
69. Li, Z.; Deng, L.; Kinloch, I.A.; Young, R.J. Raman Spectroscopy of Carbon Materials and Their Composites: Graphene, Nanotubes and Fibres. *Prog. Mater. Sci.* **2023**, *135*, 101089. [CrossRef]
70. Sadezky, A.; Muckenhuber, H.; Grothe, H.; Niessner, R.; Pooschl, U. Raman Microspectroscopy of Soot and Related Carbonaceous Materials: Spectral Analysis and Structural Information. *Carbon. N. Y.* **2005**, *43*, 1731–1742. [CrossRef]
71. Lim, G.H.; Lee, J.W.; Choi, J.H.; Kang, Y.C.; Roh, K.C. Efficient Utilization of Lignin Residue for Activated Carbon in Supercapacitor Applications. *Mater. Chem. Phys.* **2022**, *284*, 126073. [CrossRef]
72. Lu, L.; Sahajwalla, V.; Kong, C.; Harris, D. Quantitative X-Ray Diffraction Analysis and Its Application to Various Coals. *Carbon N. Y.* **2001**, *39*, 1821–1833. [CrossRef]
73. Qu, W.; Yuan, T.; Yin, G.; Xu, S.; Zhang, Q.; Su, H. Effect of Properties of Activated Carbon on Malachite Green Adsorption. *Fuel* **2019**, *249*, 45–53. [CrossRef]

74. Rimoli, M.F.d.S.; Nogueira, R.M.; Ferrarini, S.R.; de Castro, P.M.; Pires, E.M. Preparation and Characterization of Carbon from the Fruit of Brazil Nut Tree Activated by Physical Process. *Rev. Arvore* **2019**, *43*, 1–10. [CrossRef]
75. Salazar-Rabago, J.J.; Leyva-Ramos, R.; Rivera-Utrilla, J.; Ocampo-Perez, R.; Cerino-Cordova, F.J. Biosorption Mechanism of Methylene Blue from Aqueous Solution onto White Pine (*Pinus durangensis*) Sawdust: Effect of Operating Conditions. *Sustain. Environ. Res.* **2017**, *27*, 32–40. [CrossRef]
76. Homsirikamol, C.; Sunsandee, N.; Pancharoen, U.; Nootong, K. Synergistic Extraction of Amoxicillin from Aqueous Solution by Using Binary Mixtures of Aliquat 336, D2EHPA and TBP. *Sep. Purif. Technol.* **2016**, *162*, 30–36. [CrossRef]
77. Mokrzycki, J.; Magdziarz, A.; Rutkowski, P. The Influence of the Miscanthus Giganteus Pyrolysis Temperature on the Application of Obtained Biochars as Solid Biofuels and Precursors of High Surface Area Activated Carbons. *Biomass Bioenergy* **2022**, *164*, 106550. [CrossRef]
78. An, N.; Zagorscak, R.; Thomas, H.R. Adsorption Characteristics of Rocks and Soils, and Their Potential for Mitigating the Environmental Impact of Underground Coal Gasification Technology: A Review. *J. Environ. Manag.* **2022**, *305*, 114390. [CrossRef] [PubMed]
79. Costa De Souza, C.; Ciriano, M.R.; Ferreira Da Silva, E.; André De Oliveira, M.; Cesar, A.; Bezerra, S.; Marcello, A.R.; Dumont, R.; Candido Da Silva, A.; Rodrigues, A.; et al. Activated Carbon Obtained from Cardboard Tube Waste of Immersion Thermocouple and Adsorption of Methylene Blue. *Biomass Convers. Biorefinery* **2023**, *13*, 3297–3308. [CrossRef]
80. Medhat, A.; El-Maghrabi, H.H.; Abdelghany, A.; Abdel Menem, N.M.; Raynaud, P.; Moustafa, Y.M.; Elsayed, M.A.; Nada, A.A. Efficiently Activated Carbons from Corn Cob for Methylene Blue Adsorption. *Appl. Surf. Sci. Adv.* **2021**, *3*, 100037. [CrossRef]
81. Waghmare, C.; Ghodmare, S.; Ansari, K.; Dehghani, M.H.; Amir Khan, M.; Hasan, M.A.; Islam, S.; Khan, N.A.; Zahmatkesh, S. Experimental Investigation of H_3PO_4 Activated Papaya Peels for Methylene Blue Dye Removal from Aqueous Solution: Evaluation on Optimization, Kinetics, Isotherm, Thermodynamics, and Reusability Studies. *J. Environ. Manag.* **2023**, *345*, 118815. [CrossRef] [PubMed]
82. Deivasigamani, P.; Senthil Kumar, P.; Sundaraman, S.; Soosai, M.R.; Renita, A.A.; Karthikeyan, M.; Bektenov, N.; Baigenzhenov, O.; Venkatesan, D.; Kumar, J.A. Deep Insights into Kinetics, Optimization and Thermodynamic Estimates of Methylene Blue Adsorption from Aqueous Solution onto Coffee Husk (*Coffee arabica*) Activated Carbon. *Environ. Res.* **2023**, *236*, 116735. [CrossRef] [PubMed]
83. Grich, A.; Bouzid, T.; Naboulsi, A.; Regti, A.; Tahiri, A.A.; El Himri, M.; El Haddad, M. Preparation of Low-Cost Activated Carbon from Doum Fiber (*Chamaerops humilis*) for the Removal of Methylene Blue: Optimization Process by DOE/FFD Design, Characterization, and Mechanism. *J. Mol. Struct.* **2024**, *1295*, 136534. [CrossRef]
84. Hashemzadeh, F.; Ariannezhad, M.; Derakhshandeh, S.H. Evaluation of Cephalexin and Amoxicillin Removal from Aqueous Media Using Activated Carbon Produced from Aloe Vera Leaf Waste. *Chem. Phys. Lett.* **2022**, *800*, 139656. [CrossRef]
85. Nasran Nasehir Khan, M.; Firdaus Mohamad Yusop, M.; Faizal Pakir Mohamed Latiff, M.; Azmier Ahmad, M. Alteration of Tecoma Chip Wood Waste into Microwave-Irradiated Activated Carbon for Amoxicillin Removal: Optimization and Batch Studies. *Arab. J. Chem.* **2023**, *16*, 105110. [CrossRef]
86. Ali, I.; Afshinb, S.; Poureshgh, Y.; Azari, A.; Rashtbari, Y.; Feizizadeh, A.; Hamzezadeh, A.; Fazlzadeh, M. Green Preparation of Activated Carbon from Pomegranate Peel Coated with Zero-Valent Iron Nanoparticles (NZVI) and Isotherm and Kinetic Studies of Amoxicillin Removal in Water. *Environ. Sci. Pollut. Res.* **2020**, *27*, 36732–36743. [CrossRef]
87. Rodrigues, D.L.C.; Machado, F.M.; Osório, A.G.; de Azevedo, C.F.; Lima, E.C.; da Silva, R.S.; Lima, D.R.; Gonçalves, F.M. Adsorption of Amoxicillin onto High Surface Area–Activated Carbons Based on Olive Biomass: Kinetic and Equilibrium Studies. *Environ. Sci. Pollut. Res.* **2020**, *27*, 41394–41404. [CrossRef] [PubMed]
88. Shang, Z.; Hu, Z.; Huang, L.; Guo, Z.; Liu, H.; Zhang, C. Removal of Amoxicillin from Aqueous Solution by Zinc Acetate Modified Activated Carbon Derived from Reed. *Powder Technol.* **2020**, *368*, 178–189. [CrossRef]

Disclaimer/Publisher's Note: The statements, opinions and data contained in all publications are solely those of the individual author(s) and contributor(s) and not of MDPI and/or the editor(s). MDPI and/or the editor(s) disclaim responsibility for any injury to people or property resulting from any ideas, methods, instructions or products referred to in the content.